Measurement of the cross section of the $Q = 4.4398$ MeV $^{12}\mathrm{C}(n,n'\gamma)$ reaction from threshold to 16.5 MeV using γ and correlated $n-\gamma$ detection

K. J. Kelly, M. Devlin, J. M. O'Donnell, E. A. Bennett, M. Paris, and P. A. Copp

Measurement of the Cross Section of the $Q = 4.4398$ MeV ^{12}C($n,n'\gamma$) Reaction from Threshold to 16.5 MeV using γ and Correlated n-γ Detection

K. J. Kelly[1], M. Devlin[1], J. M. O'Donnell[1], E. A. Bennett[1], M. Paris[1], and P. A. Copp[1]

[1]*Los Alamos National Laboratory, Los Alamos, NM 87545, USA*

(Dated: June 23, 2023)

The $Q = 4.4398$ MeV ^{12}C($n,n'\gamma$) cross section was measured using a white incident neutron source through the detection of γ-rays only and n-γ coincidences using a segmented liquid scintillator detector array. While the n-γ technique utilized here is more generally applicable to a wide variety of neutron scattering measurements, the γ-only technique was successfully applied to this reaction to exploit the precise time resolution and high efficiency of this detection system to yield results with unprecedented statistical precision and total uncertainties $<2\%$ from reaction threshold up to 16 MeV incident neutron energy, clearly resolving many features in this reaction that were previously not well known. The γ-only and n-γ results are consistent with each other for the majority of the incident energy range covered in this work, thereby lending validation to the n-γ technique for future measurements, though significant disagreements are observed between both results and with the ENDF/B-VIII.0 nuclear data evaluation. These differences are particularly noticeable in the recently-evaluated energy range below 6.5 MeV, and also near 14 MeV where a "sawtooth"-like feature is observed similar to that in other ^{12}C $+ n$ reaction channels. Both γ-only and n-γ results are presented here with thorough covariance derivations.

I. INTRODUCTION

Owing to its presence in a wide variety of materials used everywhere from nuclear reactors and shielding, astrophysical scenarios, and everyday applications, neutron-induced reactions on carbon are among the most commonly-measured neutron-induced nuclear data. Specifically, ^{12}C has received so much attention in the nuclear data community that the ^{12}C(n,n) elastic scattering reaction is a standard from incident neutron energies, E_α, of 0.01–1.8 MeV. However, despite comprising up to 30–35% of the total ^{12}C $+ n$ cross section above $E_\alpha \approx 8$ MeV and contributing significantly to neutron transport within carbon-rich materials, inelastic neutron scattering on ^{12}C is not known nearly as well as elastic scattering. Note that here and throughout this manuscript Greek subscripts for energies like E_α are used to denote incident neutron energies to facilitate summations over these energies in covariance calculations.

The modern ENDF/B-VIII.0 [2] evaluation recently included a careful re-evaluation of the ^{12}C $+$ n system using an R-matrix formalism including the ^{12}C(n,n') reaction up to $E_\alpha = 6.5$ MeV. This was also the first ENDF/B evaluation where natural C was separated into ^{12}C and ^{13}C. However, the ^{12}C $+ n$ evaluation was heavily influenced by a preliminary γ-ray measurement [3] that required an energy shift in incident neutron energy to be used in the evaluation, and otherwise relied on measurements from ≈ 5 decades ago [4–6] with data from both Refs. [3, 6] requiring overall scaling shifts as well for use in the evaluation. Measurements above $E_\alpha = 6.5$ MeV are sparse, generally do not agree with each other, and do not appear to provide consistent guidance for evaluations at higher energies. The ENDF/B-VIII.0 evaluation from 6.5–20.0 MeV was adopted from the ENDF/B-VI.1 [7] evaluation.

Thus, given the pervasive presence of ^{12}C, the rela-tively poor agreement between literature measurements used to guide nuclear data evaluations, there is a need for new measurements of the ^{12}C(n,n') reaction.

Measurements of neutron scattering reactions typically rely on the detection of either γ rays (see, e.g., Refs. [3, 5, 6, 8]) or neutrons (n) typically with a monoenergetic incident neutron source (see, e.g., Refs. [9–12]), with some experiments measuring both neutrons in coincidence with γ rays at a small number of angles [13–15]. Measurements of γ rays only also usually rely on high-purity germanium (HPGe) detectors owing to the impressive resolution for γ-ray energy that can be achieved, though the poor time resolution and low efficiency can be an issue for these detectors. For the specific case of ^{12}C($n,n'\gamma$) and similar reactions, where there is essentially no competition for γ-ray emission from reactions other than the inelastic scattering reaction of interest (see Fig. 1), one can instead use a detection system with time resolution and detection efficiency far beyond that of HPGe detectors without worrying about downsides resulting from, e.g., poor γ-ray energy resolution typical for such detectors. Furthermore, for the case of organic scintillator detectors, it is also commonly possible to separate n and γ signals in the detectors, thereby allowing for data analysis to proceed using both γ and coincident n-γ detections.

This work summarizes two measurements of the $Q = 4.4398$ MeV ^{12}C($n,n'\gamma$) cross section, both using the same detector array but in separate experiments: one using only γ rays and another using correlated n-γ detection. The experimental setup for both experiments is described in Sec. II. Analysis procedures and covariance derivations for the γ-only data are described in Sec. III A, while the n-γ analysis and covariance are described in Sec. III B, noting the aspects of γ-related analysis that are similar between the two approaches. Results are presented side-by-side, and are compared with both
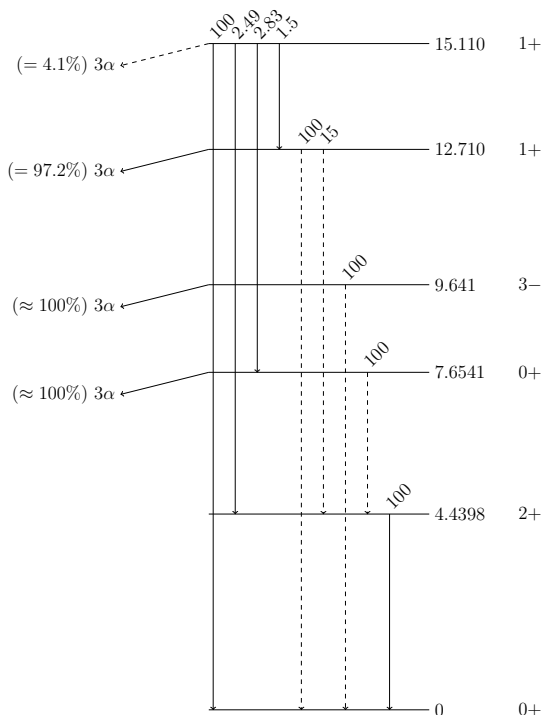
FIG. 1: The level scheme of ^{12}C based on Ref. [1], with percent branches to 3α emission shown on the left-hand side. Only the 4.4398 and 15.110 MeV levels have a significant non-3α branch. Thus, γ-only measurements are not contaminated from other inelastic excitations.

the ENDF/B-VIII.0 [2] evaluation and literature data in Sec. IV. Concluding remarks are given in Sec. V.

II. EXPERIMENTAL SETUP

Both measurements described in this work were carried out at the 15L flight path at the Weapons Neutron Research (WNR) facility at the Los Alamos Neutron Science Center (LANSCE) [17]. The WNR white neutron source is generated via spallation of 800 MeV protons incident on a tungsten target. Neutrons emitted 15° to the left of the incident proton beam were collimated and allowed to impinge on a machined graphite target of natural carbon isotopic abundance after a 21.5 m flight path. The target was an approximately 2.5 cm diameter by 2.5 cm thickness cylinder, with a total mass of approximately 26 g. The diameter of the circular profile of the incident neutron beam was 1.5 cm, and thus safely within the diameter of the target itself. The timing of the proton beam was such that a bunch of protons approximately 150 ps wide arrived every ≈ 1.778 μs, with each proton bunch producing a signal at a time, t_0, just before reaching the tungsten target. For both experiments, the graphite target was on one arm of a 3-arm target changer, developed by Rensselaer Polytechnique Institute for use in
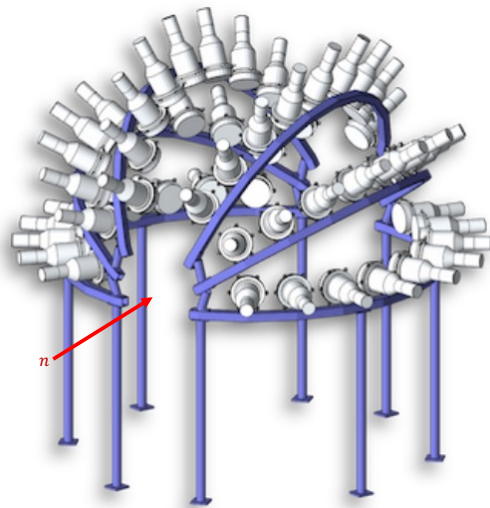
FIG. 2: A rendering of the array of liquid scintillator detectors used for the results shown in this work. Incident neutrons enter from the lower-left side of the array, and the target was placed in the center of this array. This figure is a reproduction of Fig. 3 of Ref. [16].

experiments like those described in Ref. [18] and references therein. In both experiments described here, data were collected in 10 min segments (termed "runs") with swaps between target-in and target-out positions after each run. Data runs were kept short in order to match natural variations in WNR beam intensity as closely as possible between the target-in and target-out data sets. The 15L flight path was designed specifically to reduce neutron scattering in the environment in that the nearest walls are ≥ 2 m away from the detector array, and the floor consists of a 2 m pit upon which a thin aluminum support structure holds the target and detector framework.

The detector array used for this work has previously been described in, e.g., Refs. [16, 19, 20], and the measurements described are part of the Correlated Gamma-Neutron Array for sCattering (CoGNAC) series of measurements of neutron scattering reactions at Los Alamos National Laboratory. Neutrons and γ rays for results described in this work were both detected in a 54-element EJ-309 [21] liquid scintillator array with each detector mounted to a R4144 Hamamatsu photomultiplier tube [22]. High voltages for these detectors were supplied by a CAEN SY4527 HV supply [23]. The t_0 and all liquid scintillator signals were recorded ansynchronously with a series of CAEN 1730B waveform digitizers [24] and recorded using the MIDAS data acquisition framework [25]. These detectors were in a hemispherical pattern, spanning nine angles relative to the incident neutron beam, ϑ, from 30°–150° in 15° increments. The active volume of each detector is cylindrical ≈ 7 in diameter by 2 in thick and the nominal flight path from the target

center is 1.02 m to the center of the scintillator fluid, yielding an angular coverage of $\approx \pm 5^{\circ}$ for each detector.

These liquid scintillator detectors display n-γ pulse shape discrimination (PSD) capabilities, with easily-attainable and reliable separation of neutrons and γ rays between neutron energies of ≈ 0.8–12.0 MeV (see Ref. [20] for more details). The dual n-γ detection and separation capabilities of these liquid scintillators allowed each detector to operate both as a neutron and as a γ-ray detector in separate analyses. Neutron and γ-ray signals were assigned times t_γ and t_n, respectively. PSD was used to select only γ rays for the γ-only measurements, while combinations of n-γ coincidences between all detectors were explored for the more complicated n-γ analysis approach.

Incident neutron energies, E_α, were assigned using the $t_\gamma - t_0$ time difference under the assumption that detected γ rays were those emitted from the desired ^{12}C($n,n'\gamma$) reaction and with backgrounds subtracted using different methods for each analysis approach (see Secs. III A and III B). The emitted neutron energies, E, for the n-γ analysis were assigned using the $t_n - t_\gamma$ time difference. Both E_α and E were calculated relativistically with corrections for the γ transit time where required.

The primary difference between the separate data sets used for these experiments is that the γ-only data were collected in an experimental environment that included an in-progress array of CLYC scintillators [26–28] in the lower hemisphere. Compton scattering and other γ rays do not alter the γ response of these detectors for the high $\sim$4.44 MeV γ-ray energy expected from this reaction because this energy is well-separated from other background γ rays. However, the presence of these detectors does significantly alter the net environmental neutron response of the liquid scintillators including neutron scattering in the material surrounding the detectors, and thus for now only γ rays are reported from the experimental setup including CLYC detectors.

III. DATA AND COVARIANCE ANALYSIS

Given that aspects of the γ-only analysis are contained within the n-γ analysis we first describe the γ-only analysis approach in Sec. III A, and subsequently describe the additional steps required for the n-γ analysis in Sec. III B. The most notable differences are the distinct background-subtraction techniques used for each analysis, and the neutron response treatments required for the n-γ analysis. The covariances are described alongside each analysis.

A. γ-ray Data

Following PSD selection of γ rays for each detector similar to the process described in Ref. [20], the spectrum of the integral of each liquid scintillator signal versus the
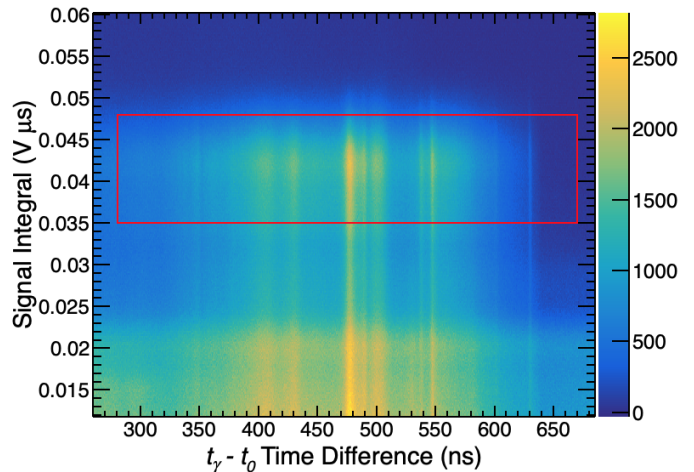
FIG. 3: (color online) The liquid scintillator signal integral versus $t_\gamma - t_0$ time difference spectrum for the γ-only analysis described in this work relative to the γ transit time. Time bins are each 0.293 ns wide.

$t_\gamma - t_0$ time difference was measured. Data with the target removed from the beam path were also collected to account for both ambient and beam-induced backgrounds. The spectrum of background-subtracted counts is shown in Fig. 3, and represents a sum over detection angle. The red rectangle in this figure represents the cut placed on the data to select γ-ray signals surrounding γ-ray energy, $E_\gamma = 4.4398$ MeV expected from the reaction of interest.

The poor pulse-integral resolution for γ-ray energy observed in these detectors ($\geq 30\%$) made the definition of this cut quite broad, but the resulting cross section was insensitive to variations $\geq 10\%$ in both the upper and lower integral limits of this cut. It is this pulse-integral resolution that typically eliminates liquid scintillators from consideration for use as a detector in γ-ray spectroscopy measurements, especially when HPGe are able to provide γ-ray energy resolution typically better than 0.1%. However, for this specific case of the ^{12}C($n,n'\gamma$) reaction, there is virtually no competition for emission of γ rays from neutron-induced reactions on ^{12}C because the ^{12}C(n,γ) capture cross section is $\approx$3 orders of magnitude smaller than this single $Q = 4.4398$ MeV inelastic reaction, and other inelastic channels lead immediately to a γ-free breakup reaction until $E_\alpha = 16.4$ MeV in the laboratory frame [2]. Thus, a gate on the E_γ range of interest, even with poor resolution, produces a clean measurement of the desired ^{12}C($n,n'\gamma$) reaction. Furthermore, given that the E_γ resolution is not an issue, the vastly improved time resolution and higher efficiency for these liquid scintillator detectors can be exploited to produce a high-statistics, high-resolution measurement of this ^{12}C($n,n'\gamma$) reaction. The 1-σ time resolution of the summed liquid scintillator array was 0.72 ns for the data set shown here, compared with time resolution the values of roughly 5–10 ns or worse that are typical of HPGe

detectors owing to the inherently slow charge-collection process utilized in these detectors [29–31].

At each γ-ray detection angle, ϑ_γ, the counts integrated within this cut on the data (target-in) spectrum, $d_\alpha(\vartheta_\gamma)$ and of the background (target-out) spectrum, $b_\alpha(\vartheta_\gamma)$ were calculated, with the α index defining the incident neutron energy. The α incident energy centroid values were defined as the average of the 0.293 ns time bin edges, relativistically converted to incident neutron energy. These were then summed over all measured angles with a $\sin(\vartheta_\gamma)$ weighting factor to create data and background sums as

$$d_{\alpha,s} = \sum_{\vartheta_\gamma} d_\alpha(\vartheta_\gamma)\sin(\vartheta_\gamma), \tag{1}$$

and

$$b_{\alpha,s} = \sum_{\vartheta_\gamma} b_\alpha(\vartheta_\gamma)\sin(\vartheta_\gamma), \tag{2}$$

respectively. Backgrounds were subtracted with a relative scaling factor based on the integral of the beam flux measured in front of the target position for data with the target in place, A_d, and with the target out, A_b. Note that no corrections for γ-ray efficiency were employed here because this work reports a cross section shape only (not magnitude), and there is only a single γ-ray energy measured for this cross section (doppler shifting of this energy was not a significant effect). Thus, assuming a constant efficiency for detection of this γ-ray energy in each near-identical liquid scintillator detector, the γ-ray efficiency amounts to a constant scaling factor that drops out of the definition of the cross section shape.

The energy spectrum of incident neutrons as measured with a ^{235}U fission chamber was used to convert the observed counts into a cross section shape. The measured counts in the ^{235}U fission chamber at incident neutron energy α, denoted φ_α, were converted to flux shape by dividing out the ^{235}U(n,f) cross section, $\sigma_{5,\alpha}$ obtained from the ENDF/B-VIII.0 nuclear data library [2] at the same incident neutron energy. These factors combine to form a shape for the ^{12}C$(n,n'\gamma)$ cross section from γ rays only, $\chi_{\gamma,\alpha}$, as

$$\chi_{\gamma,\alpha} = \left[d_{s,\alpha} - \frac{A_d}{A_b} b_{s,\alpha} \right] \frac{\sigma_{5,\alpha} w_{\varphi,\alpha}}{\varphi_\alpha w_{d,\alpha}}, \tag{3}$$

where $w_{d,\alpha}$ and $w_{\varphi,\alpha}$ are the widths of incident energy bin α in the data and flux spectra, respectively. The wide angular coverage of the detector array employed for this work resulted in negligible differences between the angle-summed data and the result obtained by integrating Legendre polynomial functions fit to the data, thus we report the angle-summed result here. The γ-ray angular distributions obtained for these data are also consistent with those already reported in Ref. [20], and so no new distributions are reported.

The factors $d_{s,\alpha}$, $b_{s,\alpha}$, and φ_α all contribute only statis-
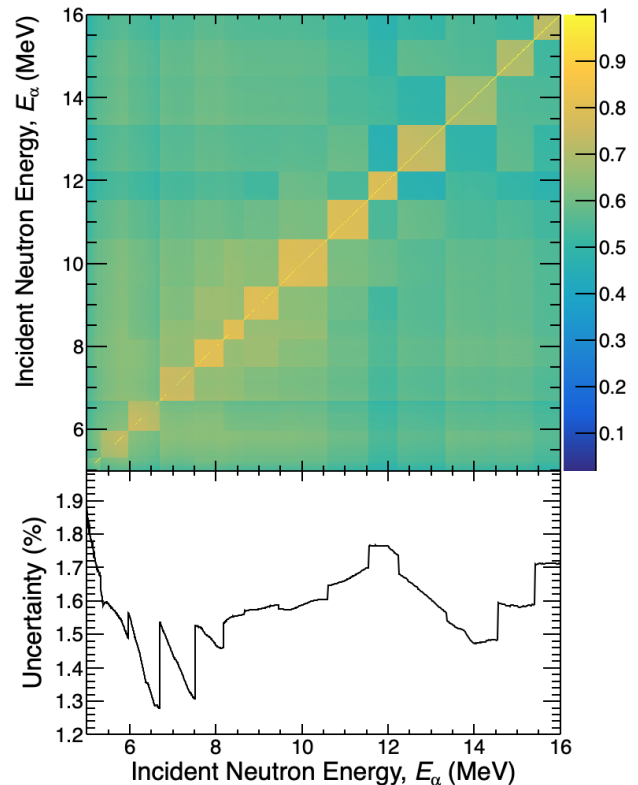
FIG. 4: (color online) The correlation matrix for the γ-only cross section results is shown in the top panel, with the 1-σ uncertainty trend shown in the bottom. The block structures in the covariance are the result of the ^{235}U(n,f) cross section. Note that the correlation matrix scale goes from 0–1, as opposed to -1–1. Thus, correlations are relatively high, and therefore the shape of this cross section is well-constrained.

tical uncertainties with no correlation between incident energies. The flux integrals, A_d and A_b, also only contribute statistical uncertainties, but they create a correlation across incident energies because they are a constant for each incident energy. However, the total statistical uncertainty of A_d and A_b are small (both less than 0.2%) as they are integrated spectra over the entire incident neutron energy of the measurement, as opposed to single counts in that spectrum. The ENDF/B-VIII.0 ^{235}U(n,f) reference cross section is the dominant source of diagonal and off-diagonal covariance for the γ-only result shown in this work.

The covariance for this result between two potentially different incident neutron energies, α and β, can be writ-

ten as

$$
\begin{aligned}
\mathrm{cov}&\big[\chi_{\gamma,\alpha},\chi_{\gamma,\beta}\big]\\
&=\;\delta_{\alpha\beta}\Bigg\{\left(\frac{\partial\chi_{\gamma,\alpha}}{\partial d_{s,\alpha}}\right)^{2}\mathrm{var}\,[d_{s,\alpha}]+\left(\frac{\partial\chi_{\gamma,\alpha}}{\partial b_{s,\alpha}}\right)^{2}\mathrm{var}\,[b_{s,\alpha}]\\
&\qquad+\left(\frac{\partial\chi_{\gamma,\alpha}}{\partial\varphi_{\alpha}}\right)^{2}\mathrm{var}\,[\varphi_{\alpha}]\Bigg\}\\
&\quad+\left(\frac{\partial\chi_{\gamma,\alpha}}{\partial A_{d}}\right)\left(\frac{\partial\chi_{\gamma,\beta}}{\partial A_{d}}\right)\mathrm{var}\,[A_{d}]\\
&\quad+\left(\frac{\partial\chi_{\gamma,\alpha}}{\partial A_{b}}\right)\left(\frac{\partial X_{\beta}}{\partial A_{b}}\right)\mathrm{var}\,[A_{b}]\\
&\quad+\left(\frac{\partial\chi_{\gamma,\alpha}}{\partial\sigma_{5,\alpha}}\right)\left(\frac{\partial\chi_{\gamma,\beta}}{\partial\sigma_{5,\alpha}}\right)\mathrm{cov}\,[\sigma_{5,\alpha},\sigma_{t,\beta}],\quad(4)
\end{aligned}
$$

where $\delta_{\alpha,\beta}$ is a Kronecker delta function. The derivatives can be obtained from Eq. (3). Lastly, given that this is a shape measurement, with the overall scaling of the cross section free to vary for any given application, the covariance must be normalized to obtain the proper shape covariance [32, 33]. Thus, the final cross section shape is given by

$$
\sigma_{\gamma,\alpha}=\chi_{\gamma,\alpha}\left[\sum_{\beta}\chi_{\gamma,\beta}\right]^{-1}=\chi_{\gamma,\alpha}A_{\gamma}^{-1},\qquad(5)
$$

with a covariance defined by [33]

$$
\begin{aligned}
\mathrm{cov}&\big[\sigma_{\gamma,\alpha},\sigma_{\gamma,\beta}\big]\\
&=\sum_{\lambda}\sum_{\omega}\left(\frac{\delta_{\alpha\lambda}}{A_{\gamma}}-\frac{\chi_{\gamma,\alpha}}{A_{\gamma}^{2}}w_{d,\lambda}\right)\\
&\quad\times\left(\frac{\delta_{\beta\omega}}{A_{\gamma}}-\frac{\chi_{\gamma,\beta}}{A_{\gamma}^{2}}w_{d,\omega}\right)\mathrm{cov}\big[\chi_{\gamma,\lambda},\chi_{\gamma,\omega}\big],\qquad(6)
\end{aligned}
$$

where λ and ω are also incident neutron energy indices in the sum. Both $\sigma_{\gamma,\alpha}$ and $\mathrm{cov}\big[\sigma_{\gamma,\alpha},\sigma_{\gamma,\beta}\big]$ are subject to the chosen overall scaling factor, and the integration range for the normalization of the cross section is dependent on the chosen application. Thus, we report the unnormalized correlation matrix and 1D uncertainty trend, shown in the top and bottom panels of Fig. 4 respectively. These can be used to obtain the covariance, which can then be normalized as desired for any given application.

B. n-γ Data

The process for selection of γ-ray signals in the n-γ analysis was identical to that of Sec. III A, and neutron signals were selected using PSD over a similar signal integral range individually for each detector. A further n-γ distinction was made using the kinematics of the neutrons emitted following γ-ray detection. As described in Sec. II, the t_0, t_γ, and t_n detection times were used to
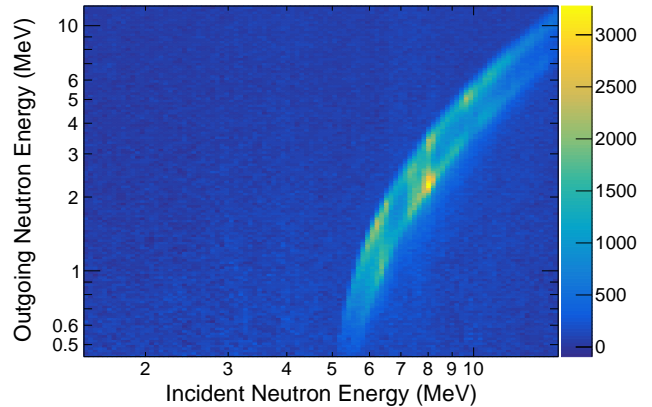
FIG. 5: (color online) The background-subtracted n-γ data are shown here, summed over all neutron detection angles. The range of outgoing neutron energies observed at each incident neutron energy corresponds to the difference in kinematics for each outgoing neutron detection angle.

define the incident and outgoing neutron energies from the scattering reaction of interest. An example of this spectrum for the $^{12}\mathrm{C}(n,n'\gamma)$ reaction is shown in Fig. 5 after background subtraction.

The primary backgrounds for coincidence data like these are from coincidences between neutrons and γ rays that are only accidentally measured to be in coincidence with each other, and are not truly originating from the same scattering reaction. A discussion of the the corrections for and the dominant origins of random coincidences from this same $^{12}\mathrm{C}(n,n'\gamma)$ reaction was given in Ref. [20]. Thus, here we only reiterate the conclusion that neutrons from the $^{12}\mathrm{C}(n,n)$ elastic scattering reaction appear to be the primary source of γ-anticoincident neutrons contributing to the random-coincidence background in these data. These backgrounds were removed from the data shown in Fig. 5 using the methods of Refs. [34, 35], leaving only the desired signals of interest. No additional target-out background measurements were required for this method.

As opposed to the effectively monoenergetic γ-ray measurement utilized for the analysis in Sec. III A, yielding a constant detection efficiency term that does not impact the shape of the obtained cross section, the energy of neutrons emitted from scattering reactions changes with the incident neutron energy, and thus an understanding of the detection efficiency and difference in the environmental response of each neutron energy is required. While a 1D neutron detection efficiency curve was appropriately applied in Ref. [20] to obtain n, γ, and correlated n-γ distributions, 1D efficiency curves are not generally applicable for neutron measurements [38] unless well-separated bands of neutrons are available as in the case of the $^{12}\mathrm{C}(n,n'\gamma)$ data shown in this work. Even in this case, a measurement of the neutron detection efficiency using,
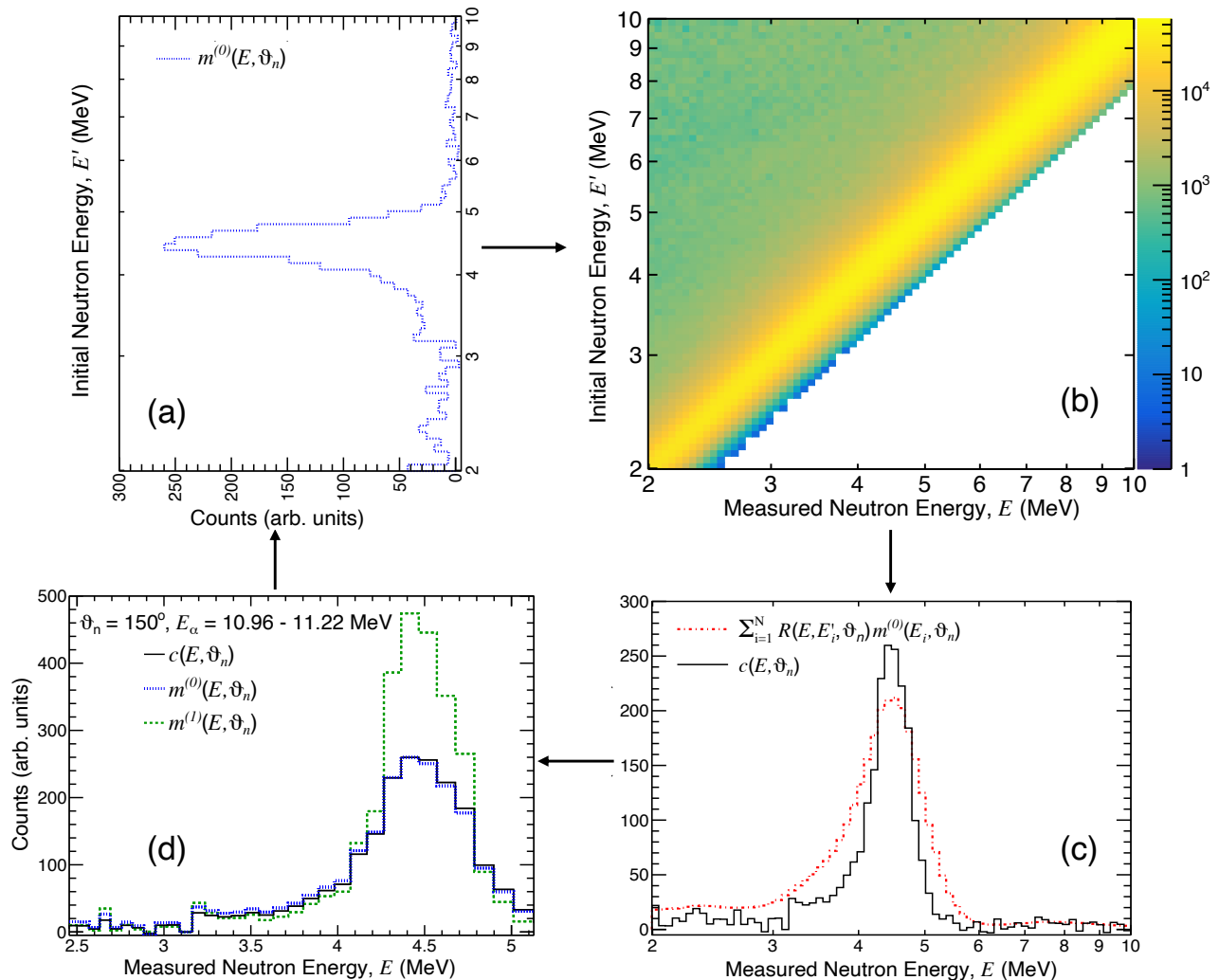
FIG. 6: (color online) A schematic for the unfolding procedure shown in Eq. (7), demonstrated using data for $E_\alpha = 10.96$–11.22 MeV and $\vartheta_n = 150°$. In panel (a) an initial guess is defined as $m^{(0)}(E, \vartheta_n)$ (blue, dotted line) from Eq. (8), which is used to scale each initial neutron energy (row) of the liquid scintillator neutron environmental response matrix [19, 36, 37] shown in panel (b). This matrix is projected into a measured neutron energy spectrum (x axis) to obtain the summation in the denominator of Eq. (7) (red, dash-dotted line) in panel (c). The ratio of background subtracted counts [$c(E, \vartheta_n)$; black, solid line] to this projection is used as a correction to $m^{(0)}(E, \vartheta_n)$ to obtain $m^{(1)}(E, \vartheta_n)$ (green, dashed line) in panel (d). This process can iterate indefinitely, though only a single iteration was required here.

e.g., a ^{252}Cf spontaneous fission neutron source (a common technique, see Ref. [39] and references therein) does not yield the correct efficiency because of the scattering of higher-energy neutrons to longer times of flight, and therefore lower measured neutron energies, in the process known as "downscattering". Thus, in Ref. [20] an MCNP[®,1]-based efficiency for measuring neutrons of a known energy was used [40, 41].

Even though a 1D curve could be applicable to these data for the same reasons as in Ref. [20], in this work we instead apply an iterative unfolding technique [38, 42] employing an MCNP-based description of the entire neutron environmental response through a 2D matrix called the response matrix, $\mathcal{R}(E, E', \vartheta_n)$ [36, 37], where ϑ_n is

---

the neutron detection angle. The response matrix describes the distortion of the initial neutron energy as emitted from the target, E', to a distribution of measured neutron energies, E, typically obtained through time of flight. The response matrix used for this work is based heavily on the detailed and verified MCNP simulation of the Chi-Nu liquid scintillator experimental environment [16, 19, 37, 43], which is identical to the experimental environment for the n-γ data acquisition environment with the only exceptions being in the region of the graphite target; the in-progress CLYC detector array discussed in Sec. III A was not present during collection of these data. Thus, the MCNP description of the neutron response in the environment is believed to be accurate.

The iterative unfolding method applied here can be expressed at each neutron detection angle, ϑ_n, after summing the data over γ angle, ϑ_γ, as [38, 42]

$$m^{(n+1)}(E, \vartheta_n) = m^{(n)}(E, \vartheta_n)$$
$$\times \left[\frac{c(E, \vartheta_n)}{\sum_{i=1}^{N} \mathcal{R}(E, E'_i, \vartheta_n) m^{(n)}(E_i, \vartheta_n)} \right], \quad (7)$$

where n is the iteration number of the unfolding procedure, N is the total number of initial neutron energies considered in $\mathcal{R}(E, E', \vartheta_n)$, $c(E, \vartheta_n)$ is the counts at the measured energy E and ϑ_n, and $m^n(E, \vartheta_n)$ is the unfolding measurement result at iteration n. The 0th-order guess, $m^0(E, \vartheta_n)$, is obtained by simply dividing $c(E, \vartheta_n)$ by the y-axis (E') projection of the response matrix, to represent division of $c(E, \vartheta_n)$ by a 1D neutron detection efficiency curve, $\varepsilon(E, \vartheta_n)$, i.e.

$$m^{(0)}(E, \vartheta_n) = c(E, \vartheta_n)/\varepsilon(E, \vartheta_n). \quad (8)$$

The sum in the denominator of Eq. (7) represents the sum of contributions to the the counts observed at energy E and angle ϑ_n, based on $\mathcal{R}(E, E', \vartheta_n)$ and scaled by $m^{(n)}(E', \vartheta_n)$. If the result at iteration n is correct, then the ratio in square brackets in Eq. (7) will be unity. However, if $m^{(n)}(E, \vartheta_n)$ is not correct, then the ratio in square brackets represents a correction applied to $m^{(n)}(E, \vartheta_n)$ to obtain $m^{(n+1)}(E, \vartheta_n)$. Provided that $\varepsilon(E, \vartheta_n)$ is reasonably accurate, this unfolding approach quickly reaches an accurate answer in 1-2 iterations [38]. Only a single iteration was used to obtain the n-γ results shown in this work. This procedure is shown schematically in Figs. 6(a)–6(d).

This unfolding method corrects for efficiency just as a proper 1D efficiency curve could, but also extracts the yield of all neutrons relating to the ^{12}C$(n,n'\gamma)$ reaction at each incident energy, instead of just those at the peak of the response function for each outgoing neutron energy. This method is generally applicable to more complicated cases of overlapping resonances and even continuous distributions of neutron energy because it corrects the data for the virtually inevitable effects of neutron scattering in the environment, though there are no competing reac-

tion channels from which to downscatter into the data of interest in the case of the present work with no notable changes observed in subsequent iterations besides the enhancement of noise typical of unfolding techniques. Additionally, a significant advantage of this unfolding method over, e.g., Monte Carlo-based unfolding techniques is that it is entirely analytical, and so covariances can be directly propagated through each iteration of the unfolding procedure as opposed to generating posterior distributions or other quantities to estimate the uncertainty of the unfolded result.

Replacing $m^{(0)}(E, \vartheta_n)$ with the definition described in Eq. (8), the equation for obtaining the final results from the n-γ analysis method from the first iteration of the unfolding method at each angle can be rewritten as

$$m^{(1)}(E, \vartheta_n) = \left[\frac{c^2(E, \vartheta_n)}{\varepsilon(E, \vartheta_n)} \right]$$
$$\times \left[\sum_{i=1}^{N} \mathcal{R}(E, E_i, \vartheta_n) \frac{c(E_i, \vartheta_n)}{\varepsilon(E_i, \vartheta_n)} \right]^{-1}. \quad (9)$$

Given that the background-subtracted counts, $c(E, \vartheta_n)$, are not correlated with $\varepsilon(E, \vartheta_n)$ or $\mathcal{R}(E, E_i, \vartheta_n)$, and ignoring the covariance between $\varepsilon(E, \vartheta_n)$ and $\mathcal{R}(E, E_i, \vartheta_n)$, the covariance of $m^{(1)}(E, \vartheta_n)$ is then generally expressed as

$$\text{cov}\left[m^{(1)}(E_i, \vartheta_n), m^{(1)}(E_j, \vartheta_n) \right]$$
$$= \sum_{k,l} \left\{ \left(\frac{\partial m^{(1)}(E_i, \vartheta_n)}{c(E_k, \vartheta_n)} \right) \text{cov}\left[c(E_k, \vartheta_n), c(E_l, \vartheta_n) \right] \right.$$
$$\left. \times \left(\frac{\partial m^{(1)}(E_j, \vartheta_n)}{c(E_l, \vartheta_n)} \right) \right\}$$
$$+ \sum_{k,l} \left\{ \left(\frac{\partial m^{(1)}(E_i, \vartheta_n)}{\varepsilon(E_k, \vartheta_n)} \right) \text{cov}\left[\varepsilon(E_k, \vartheta_n), \varepsilon(E_l, \vartheta_n) \right] \right.$$
$$\left. \times \left(\frac{\partial m^{(1)}(E_j, \vartheta_n)}{\varepsilon(E_l, \vartheta_n)} \right) \right\}$$
$$+ \sum_{k,l} \left\{ \left(\frac{\partial m^{(1)}(E_i, \vartheta_n)}{\mathcal{R}(E_i, E'_k, \vartheta_n)} \right) \right.$$
$$\times \text{cov}\left[\mathcal{R}(E_i, E'_k, \vartheta_n), \mathcal{R}(E_j, E'_l, \vartheta_n) \right]$$
$$\left. \times \left(\frac{\partial m^{(1)}(E_j, \vartheta_n)}{\mathcal{R}(E_j, E'_l, \vartheta_n)} \right) \right\}. \quad (10)$$

However, the covariance of all three parameters is treated

as purely statistical, and therefore diagonal, thus

$$
\begin{aligned}
\mathrm{cov}&\big[m^{(1)}(E_i,\vartheta_n),m^{(1)}(E_j,\vartheta_n)\big]\\
&= \sum_k \left\{\left(\frac{\partial m^{(1)}(E_i,\vartheta_n)}{c(E_k,\vartheta_n)}\right)\mathrm{var}\,[c(E_k,\vartheta_n)]\right.\\
&\qquad\left.\times\left(\frac{\partial m^{(1)}(E_j,\vartheta_n)}{c(E_k,\vartheta_n)}\right)\right\}\\
&+ \sum_k \left\{\left(\frac{\partial m^{(1)}(E_i,\vartheta_n)}{\varepsilon(E_k,\vartheta_n)}\right)\mathrm{var}\,[\varepsilon(E_k,\vartheta_n)]\right.\\
&\qquad\left.\times\left(\frac{\partial m^{(1)}(E_j,\vartheta_n)}{\varepsilon(E_lk\vartheta_n)}\right)\right\}\\
&+ \sum_k \left\{\delta_{i,j}\left(\frac{\partial m^{(1)}(E_i,\vartheta_n)}{\mathcal{R}(E_i,E_k',\vartheta_n)}\right)^2\right.\\
&\qquad\left.\times\,\mathrm{var}\,[\mathcal{R}(E_i,E_k',\vartheta_n)]\right\},
\end{aligned}
\tag{11}
$$

with the $\delta_{i,j}$ term again representing a Kronecker delta function. The derivatives in Eq. (11) are given by

$$
\begin{aligned}
\frac{\partial m^{(1)}(E_i,\vartheta_n)}{c(E_k,\vartheta_n)} &= \delta_{ik}\frac{2m^{(1)}(E_i,\vartheta_n)}{c(E_i,\vartheta_n)}\\
&\quad - m^{(1)}(E_i,\vartheta_n)\frac{\mathcal{R}(E_i,E_k',\vartheta_n)}{\varepsilon(E_k,\vartheta_n)}\\
&\quad \times\left[\sum_{i=1}^{N}\mathcal{R}(E,E_i,\vartheta)\frac{c(E_i,\vartheta)}{\varepsilon(E_i,\vartheta)}\right]^{-1},
\end{aligned}
\tag{12}
$$

$$
\begin{aligned}
\frac{\partial m^{(1)}(E_i,\vartheta_n)}{\varepsilon(E_k,\vartheta_n)} &= -\delta_{ik}\frac{m^{(1)}(E_i,\vartheta_n)}{\varepsilon(E_i,\vartheta_n)}\\
&\quad + m^{(1)}(E_i,\vartheta_n)\mathcal{R}(E_i,E_k',\vartheta_n)\frac{c(E_k,\vartheta_n)}{\varepsilon^2(E_k,\vartheta_n)}\\
&\quad \times\left[\sum_{i=1}^{N}\mathcal{R}(E,E_i,\vartheta)\frac{c(E_i,\vartheta)}{\varepsilon(E_i,\vartheta)}\right]^{-1},
\end{aligned}
\tag{13}
$$

and

$$
\begin{aligned}
\frac{\partial m^{(1)}(E_i,\vartheta_n)}{\mathcal{R}(E_j,E_k,\vartheta_n)} &= -\delta_{ij}\frac{m^{(1)}(E_i,\vartheta_n)c(E_i,\vartheta_n)}{\varepsilon(E_i,\vartheta_n)}\\
&\quad \times\left[\sum_{i=1}^{N}\mathcal{R}(E,E_i,\vartheta)\frac{c(E_i,\vartheta)}{\varepsilon(E_i,\vartheta)}\right]^{-1}.
\end{aligned}
\tag{14}
$$

Equations (11)–(14) describe the covariance between all outgoing energy, E, data points for each E_α and ϑ_n in the unfolded version of spectra like that shown in Fig. 5. Similar to the analysis in Sec. III A, the only sources of cross-ϑ_n correlations are the flux counts, φ_α, and the ^{235}U(n,f) reference cross section, $\sigma_{5,\alpha}$ because they are the same for each E_α regardless of ϑ_n. However, at each
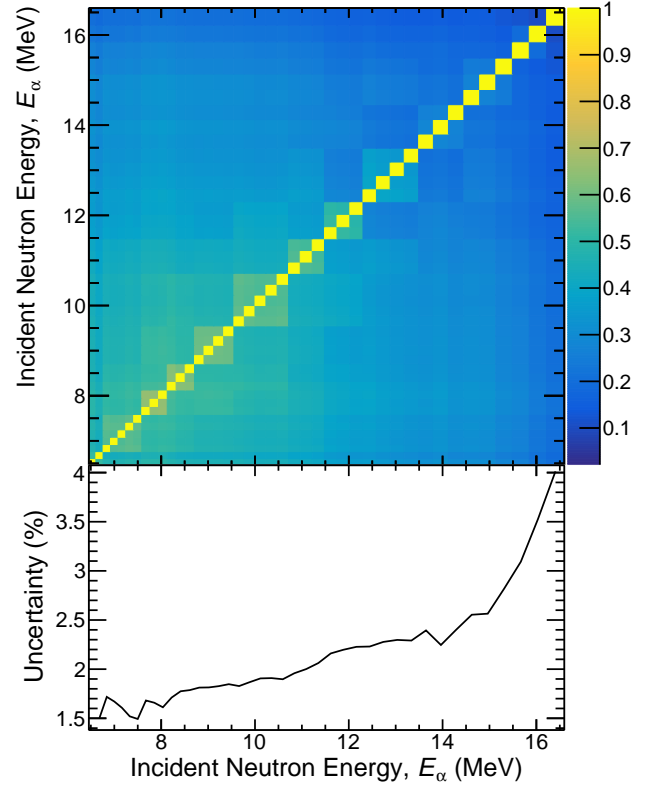
FIG. 7: (color online) The correlation matrix for the unnormalized n-γ cross section results is shown in the top panel, with the 1-σ uncertainty trend shown in the bottom. Again, the block structures in the covariance are the result of the ^{235}U(n,f) cross section, and the correlation matrix scale goes from 0–1, as opposed to -1–1.

E_α this only produces a magnitude shift with a systematic uncertainty that is constant across ϑ_n, which does not impact the relative angular distribution integrated at each E_α. Thus, φ_α and $\sigma_{5,\alpha}$ are not explicitly included until later in the covariance calculation.

For each ϑ_n, unfolded counts for the excitation band corresponding to the ^{12}C$(n,n'\gamma)$ reaction of interest were summed over 95% (Gaussian 2 σ) of the energy range corresponding to the expected outgoing neutron energy at each E_α, calculated using relativistic kinematics. The results of this analysis are nearly identical when anywhere from 80–99% of the distribution of counts observed at each E_α-ϑ_n combination is included. The summed counts at each ϑ_n, defined as $W_{n\gamma,\alpha}(\vartheta_n)$, and the associated covariance are described by

$$
W_{n\gamma,\alpha}(\vartheta_n) = \sum_{x=\mathrm{low}}^{\mathrm{high}} m^{(1)}_\alpha(E_x,\vartheta_n)w(E_x),
\tag{15}
$$

where $w(E_i)$ is the logarithmically-spaced bin width of

the outgoing energy bin at E_i, and

$$
\begin{aligned}
&\text{cov}\big[W_{n\gamma,\alpha}(E_i,\vartheta_n), W_{n\gamma,\alpha}(E_j,\vartheta_n)\big] \\
&= \sum_{k,l} \left(\frac{\partial W_{n\gamma,\alpha}(E_i,\vartheta_n)}{m_\alpha^{(1)}(E_k,\vartheta_n)}\right)\left(\frac{\partial W_{n\gamma,\alpha}(E_j,\vartheta_n)}{m_\alpha^{(1)}(E_l,\vartheta_n)}\right), \\
&\quad \times \text{cov}\big[m_\alpha^{(1)}(E_k,\vartheta_n), m_\alpha^{(1)}(E_l,\vartheta_n)\big] \\
&= \sum_{k,l} w(E_k)w(E_l)\text{cov}\big[m_\alpha^{(1)}(E_k,\vartheta_n), m_\alpha^{(1)}(E_l,\vartheta_n)\big]
\end{aligned}
\tag{16}
$$

At this point, the normalized angular distribution could be calculated from the $\chi_\alpha(\vartheta_n)$ values. The n, γ, and correlated n-γ distributions from this same reaction and the same raw experimental data were already published in Ref. [20], though the analysis here is different than that of Ref. [20] because of the new application of the unfolding technique to the data. The distributions obtained from this analysis are nearly identical to those of Ref. [20], and so they are not reported again here.

The integral of the $W_{n\gamma,\alpha}(\vartheta_n)$ distributions scaled by the flux details produce the desired cross section shape, $\chi_{n\gamma,\alpha}$ as

$$
\chi_{n\gamma,\alpha} = \sum_j W_{n\gamma,\alpha}(\vartheta_{n,j})sin(\vartheta_{n,j})\frac{\sigma_{5,\alpha}}{\varphi_\alpha}.
\tag{17}
$$

As with the γ-only analysis, φ_α are the counts observed in the ^{235}U flux monitor at incident energy, E_α, and $\sigma_{5,\alpha}$ is the ENDF/B-VIII.0 [2] ^{235}U(n,f) cross section at the same energy. The distance from the flux monitor to the tungsten spallation target was determined to ± 1.5 cm (0.08%), and does not impact the uncertainty of the final result. The full covariance of the ENDF/B-VIII.0 ^{235}U(n,f) cross section was included as well, as should be expected from its use as a reference.

Finally, as with the γ-only analysis, the cross section shape must be properly normalized before scaling to a chosen cross section magnitude. Thus,

$$
\sigma_{n\gamma,\alpha} = \chi_{n\gamma,\alpha}\left[\sum_\beta \chi_{n\gamma,\beta}\right]^{-1} = \chi_{n\gamma,\alpha}A_{n\gamma}^{-1},
\tag{18}
$$

with a covariance defined by identically as in Eq. (6), and $\chi_{n\gamma,\alpha}$ covariances defined trivially from Eq. (17).

The correlation matrix corresponding to the covariance of $\chi_{n\gamma,\alpha}$ is shown in Fig. 7, with the 1D uncertainty trend shown in the bottom panel.

IV. RESULTS

The results for the γ-only and n-γ analyses are shown in Fig. 8(a) in cyan and black, respectively, compared with literature measurements [5, 6, 10–12], and a cluster of measurements near $E_\alpha \approx 14$ MeV shown as a single color since there are a large number of such measure-ments at only this energy [45–50]. As described earlier, the energy binning of the γ-only data is based on 0.293 ns bins of total time of flight. The n-γ results are logarithmically binned at 100 bins per decade in order to approximately increase energy bin widths with decreasing incident neutron flux at higher incident energies. It is anticipated that the binning for both γ-only and n-γ results will remain consistent for all results in the the the CoGNAC neutron scattering measurement campaign to facilitate comparisons of results between different isotopes, which proved useful during, for example, the Chi-Nu series of prompt fission neutron spectrum measurements [16, 19]. We also show enhanced plots of the results in Figs. 8(b)–8(e) to show the detail of the results of this work. For nuclear data evaluations, we focus on comparisons with the ENDF/B-VIII.0 [2] evaluation because other leading evaluation libraries either have only a natural C library as is the case with the JEFF-3.3 evaluation [51], are identical to outdated ENDF/B evaluations of natural C as with both the CENDL-3.2 and JEFF-3.3 libraries [51, 52], or is adopted directly from a decades-old natural C evaluation as with the JENDL-5.0 library [53].

Before discussing comparisons with previous work, we clarify the state of the ENDF/B-VIII.0 evaluation [2] regarding this cross section. (See Ref. [2, Sec. III.8] for a more detailed description of the R-matrix evaluation.) The ENDF/B-VIII.0 evaluation for the neutron sublibrary of ^{12}C from thermal incident neutron energies to 6.5 MeV is based on an R-matrix analysis of the ^{13}C system. This analysis included 21 channels in three partitions, each with a potentially-unique maximum orbital angular momentum, ℓ_{max}: $n+^{12}$C with $\ell_{max} = 4$, $n+^{12}$C* with $\ell_{max} = 1$, and $\gamma+^{13}$C with $\ell_{max} = 1$. Above this energy, information from the 1991 ENDF/B-VI.1 evaluation [7] was joined to the lower-energy R-matrix evaluation. The data used in ENDF/B-VIII.0 for this reaction were those of Galati et al. [4] and Rogers et al. [5], with normalization factors unchanged from their published values. Additionally, data from Wender et al. [6] and Negret et al. [3] were used in this evaluation, but were rescaled with energy-independent normalization factors of 1.112 and 0.868, respectively. These normalization factors were adjusted as parameters in the R-matrix generalized least squares fitting procedure [54]. The data from Negret et al. were also shifted in energy by -58 keV, which was reflective of the preliminary status of this data in the preparation of the ENDF/B-VIII.0 evaluation. Instead, in this work we compare with an updated data set from the same author [44] for a portion of their reported incident energy range in Fig. 8(b). Although no additional scaling or shifts were applied to these data, we emphasize that they are also preliminary [44]. The choice of scaling the Wender et al. [6] data set for use in ENDF/B-VIII.0 was maintained in Fig. 8(b) for comparison with the present results.

Beginning with the E_α range shown in Fig. 8(b), where ENDF/B-VIII.0 was recently updated, we see significant differences in shape and strength of various resonance
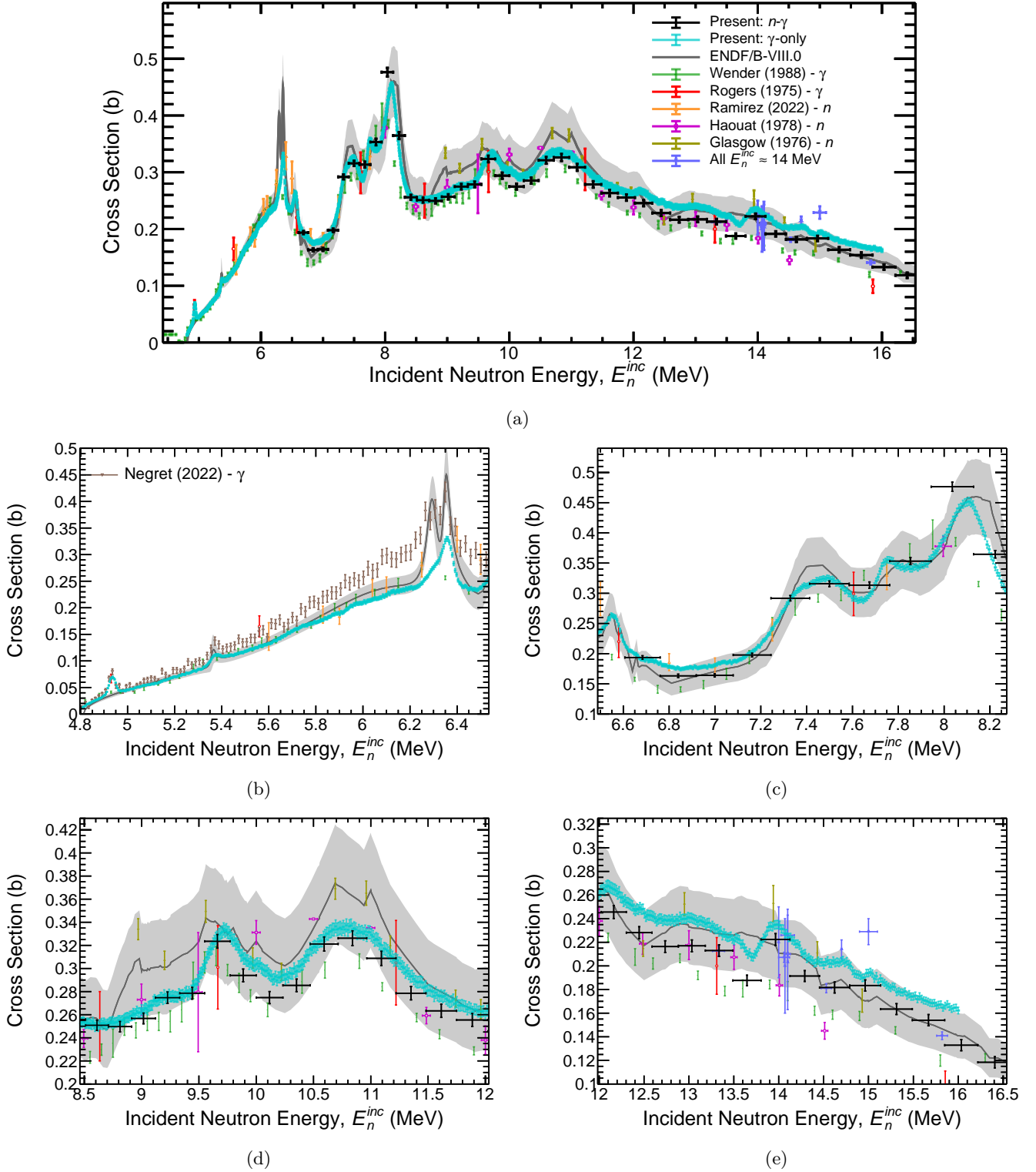
FIG. 8: (color online) The present *n*-γ and γ-only cross section results are shown as the black and cyan data points, respectively, for the entire measured energy range in (a), and from 4.80–6.50 MeV in (b), 6.5–8.25 MeV in (c), 8.25–12.0 MeV in (d), and 12.0–16.5 MeV in (e). The ENDF/B-VIII.0 evaluation is shown as the black, solid line with the gray shaded region representing the evaluation uncertainties, and literature data are described in the legend, along with the type of measurement (either γ or *n* for literature data). The preliminary data from Negret *et al.* [3, 44] are shown here as the open, brown triangles in Fig. 8(b).

features. First, the $9/2^+$ resonance at 4.85 MeV, which was excluded from ENDF/B-VIII.0 because there was no clear evidence of its existence, is now clearly observed with roughly 15 data points mapping the peak shape on either side. Conversely, the $7/2^-$ resonance at approximately 6.28 MeV is nearly nonexistent in the present results, seen only as a small feature on the low-energy side of the next resonance, $5/2^-$, at 6.35 MeV. The literature data are roughly in agreement with the present results, though the Wender *et al.* data trend lower than the present results in general (recall that these data were scaled up by a factor of 1.112) and Negret *et al.* data trend higher for most of this E_α range. The E_α range in this plot is also the only range where we observe significant disagreements with ENDF/B-VIII.0 outside of the uncertainty of the evaluation, though we note that the ENDF/B-VIII.0 uncertainties in this range are much smaller than for all higher E_α values.

In Fig. 8(c), both γ-only and n-γ data sets are again roughly in agreement with each other, and existing literature data sets. The ENDF/B-VIII.0 evaluation in this range appears to contain resonances in approximately the correct placement and relative magnitudes, though the shapes of these features are generally too coarse. On the other hand, Fig. 8(d) shows a pretty clear disagreement between in the cross section magnitude and shape between the present results and ENDF/B-VIII.0. The literature data loosely support the shape of the present results over ENDF/B-VIII.0, with the exception of data from Glasgow *et al.* [12]. In Fig. 8(e) the γ-only and n-γ data are slightly offset from each other in magnitude, with the n-γ data trend closer to ENDF/B-VIII.0 and Wender *et al.* data, and γ-only data trending closer to the data from Glasgow *et al.*. This disagreement may only be the result of a slight error in the magnitude of these results, which is variable considering that these are shape data [33]. It is also possible that and additional background from γ-ray decays of the 12.710 MeV level in ^{12}C is entering into the γ-only data analysis above the approximately 13.8 MeV laboratory energy threshold for excitation of this state, but this would not account for differences between these results in the E_α = 12–13.8 MeV range.

In Fig. 8(e) we emphasize the fact that both γ-only and n-γ results show a distinct "sawtooth" feature near E_α = 14 MeV, which raises questions regarding the precise incident energy centroid and width of neutron beams utilized for the cluster of measurements near E_α = 14 MeV. Interestingly, distinct features were also observed in ^{12}C(n,α_0) reaction data from Ref. [55] at approximately the same energies, again adding uncertainty to measurements near E_α = 14 MeV for this and potentially other ^{12}C + n reactions. Despite some differences at various E_α values, both γ-only and n-γ data presented in this work agree within uncertainties for nearly the entire E_α range shown in Figs. 8(c)–8(e), though the total uncertainty in the present results are sometimes an order of magnitude smaller than the ENDF/B-VIII.0 result

and with a much finer E_α grid in the case of the γ-only results.

Finally, we note that the ENDF/B-VIII.0 evaluation was recently updated to now include 40 channels over the same three partitions as in the evaluation for ENDF/B-VIII.0 but the $\ell_{\max}$ for the $n+^{12}$C* partition was increased to 3 from its previous value of 1. The increase in $\ell_{\max}$ allows the evaluation to access the $J^\pi = 9/2^+$ resonance at $E_\alpha \approx$ 4.95 MeV, which is not present in ENDF/B-VIII.0 in Fig. 8(b). However, the present results were not yet included in this updated evaluation, and so the shape of this resonance does not yet match the data. This new R-matrix evaluation resulted in slightly different normalization factors for the data in Refs. [44] and [6] (0.862 and 1.115, respectively) compared to those of ENDF/B-VIII.0. Despite these changes, the disagreements between ENDF/B-VIII.0 and the present results in the 6.2–6.4 MeV range are largely unchanged in the new evaluation, though these features in ENDF/B-VIII.0 may be artifacts of the lower resolution of previous measurements. The present measurements indicate the need to further re-evaluate the ^{13}C system and this work is currently underway.

V. CONCLUSIONS

In this work we report results from two separate measurements of the Q = 4.4398 MeV ^{12}C$(n,n'\gamma)$ reaction, both of which were carried out at the WNR facility at LANSCE using a segmented liquid scintillator detector array. An unprecedented high precision on incident neutron energy and low statistical uncertainty on the final result was obtained using measurements of γ rays only. An n-γ coincidence measurement of the same reaction was also obtained, with results that are consistent with the γ-only measurement for the majority of the measured energy range. With the exception of energies up to approximately 1.5 MeV above the reaction threshold, both measurements agree within ENDF/B-VIII.0 evaluation uncertainties and broadly agree with literature, though there are many notable structural differences between the present results and both literature data and evaluations. The most significant differences appear to be the omission of a resonance at approximately 4.85 MeV in ENDF/B-VIII.0, a generally different cross section structure from 8.5–11 MeV, and the existence of a "sawtooth" feature in the cross section near 14 MeV. This latter feature is particularly interesting because (a) it appears to be present in some form in other ^{12}C + n reactions, and (b) it calls into question the fine details of incident neutron beams used for the large number of measurements that were carried out *only* near this energy.

While the γ-only result shown in this work is far superior to the n-γ result, the high efficiency and narrow time resolution allowing for this quality of result can only be exploited for special cases, with the poor energy resolution of these detectors hindering their use in this way for

most other measurements. The n-γ technique employed here is more generally applicable, and should be able to produce impactful results on a wide variety of other nuclei.

VI. ACKNOWLEDGEMENTS

[1] J. H. Kelley, J. E. Purcell, and C. G. Sheu, Nucl. Phys. A **71**, 968 (2017).

[2] D. A. Brown, M. B. Chadwick, R. Capote, A. C. Kahler, A. Trkov, *et al.*, Nucl. Data Sheets **148**, 1 (2018).

[3] A. Negret, C. Borcea, P. Dessagne, M. Kerveno, N. Nankov, *et al.*, Nucl. Data. Sheets **119**, 179 (2014).

[4] W. Galati, J. D. Brandenberger, and J. L. Weil, Phys. Rev. C **5**, 1508 (1972).

[5] V. C. Rogers, V. J. Orphan, C. G. Hoot, and V. V. Verbinski, Nucl. Sci. Eng. **58**, 298 (1975).

[6] S. A. Wender, S. J. Seestrom-Morris, and R. O. Nelson, J. Phys. G: Nucl. Phys. **14**, S417 (1988).

[7] P. F. Rose, Brookhaven National Laboratory Report BNL-NCS-17541 (1991).

[8] A. Negret, C. Borcea, P. Dessagne, M. Kerveno, A. Olacel, *et al.*, Phys. Rev. C **034602**, 90 (2014).

[9] A. P. D. Ramirez, J. R. Vanhoy, S. F. Hicks, M. T. McEllistrem, E. E. Peters, *et al.*, Phys. Rev. C **95**, 064605 (2017).

[10] A. P. D. Ramirez, E. E. Peters, J. R. Vanhoy, S. F. Hicks, L. A. Alasgas, *et al.*, Nucl. Phys. A **122446**, 1023 (2022).

[11] G. Haouat, J. Lackhar, J. Sigaud, Y. Patin, and Coçu, Nucl. Sci. Eng. **65**, 331 (1978).

[12] D. W. Glasgow, F. O. Purser, H. Hogue, J. C. Clement, K. Stelzer, and otheres, Nucl. Sci. Eng. **61**, 521 (1976).

[13] R. C. Haight, J. M. O'Donnell, L. Zanini, M. Devlin, and D. Rochman, LA-UR-02-5486 (2002).

[14] D. Rochman, R. C. Haight, J. M. O'Donnell, M. Devlin, T. Ethvignot, and T. Granier, Nucl. Instrum. Methods A **523**, 102 (2004).

[15] D. Rochman, R. C. Haight, J. M. O'Donnell, M. Devlin, T. Ethvignot, *et al.*, AIP Conf. Proc. **769**, 985 (2005).

[16] K. J. Kelly, J. A. Gomez, M. Devlin, J. M. O'Donnell, D. Neudecker, *et al.*, Phys. Rev. C **105**, 044615 (2022).

[17] P. W. Lisowski and K. F. Schoenberg, Nucl. Instrum. Methods A **562**, 910 (2006).

[18] K. S. Mohindroo, Y. Danon, E. Blain, M. Devlin, and K. J. Kelly, Ann. Nucl. Energy **165**, 108647 (2022).

[19] K. J. Kelly, M. Devlin, J. M. O'Donnell, J. A. Gomez, D. Neudecker, *et al.*, Phys. Rev. C **102**, 034615 (2020).

[20] K. J. Kelly, M. Devlin, J. M. O'Donnell, and E. A. Bennett, Phys. Rev. C **104**, 064614 (2021).

[21] https://eljentechnology.com/products/liquid-scintillators/ej-301-ej-309.

[22] https://www.hamamatsu.com.

[23] https://www.caen.it/products/sy4527 (2020).

[24] https://www.caen.it/products/v1730 (2020).

[25] https://midas.triumf.ca.

[26] J. Glodo, E. van Loef, R. Hawrami, W. M. Higgins, A. Churilov, *et al.*, IEEE Trans. Nucl. Science **58**, 333 (2011).

[27] K. J. Kelly, E. A. Bennett, M. Devlin, J. M. O'Donnell, and M. Paris, Proc. of the 15th International Conference on Nuclear Data for Science and Technology (ND2022), Accepted (2023).

[28] E. A. Bennett, K. J. Kelly, M. Devlin, and J. M. O'Donnell, Nucl. Instrum. Methods A, In Prog. (2023).

[29] J. A. Becker, L. A. Bernstein, W. Younes, D. P. McNabb, P. E. Garrett, *et al.*, J. Nucl. Sci. Technology **S2**, 620 (2002).

[30] R. O. Becker, J. A. ann Nelson, AIP Conf. Proc. **769**, 748 (2005).

[31] G. Knoll, *Radiation Detection and Measurements* (John Wiley and Sons, 1996).

[32] D. Neudecker, R. Capote, D. L. Smith, T. Burr, and P. Talou, Nucl. Sci. Eng. **179**, 381 (2015).

[33] K. J. Kelly, J. M. O'Donnell, D. Neudecker, M. Devlin, and J. A. Gomez, Nucl. Instrum. and Methods A **943**, 162449 (2019).

[34] J. M. O'Donnell, Nucl. Instrum. Methods A **805**, 87 (2016).

[35] K. J. Kelly, J. M. O'Donnell, J. A. Gomez, M. Devlin, and E. A. Bennett, Nucl. Instrum. Methods A **1045**, 167531 (2023).

[36] K. J. Kelly, J. M. O'Donnell, J. A. Gomez, T. N. Taddeucci, M. Devlin, *et al.*, Nucl. Instrum. and Methods A **866**, 182 (2017).

[37] T. N. Taddeucci, R. C. Haight, H. Y. Lee, D. Neudecker, J. M. O'Donnell, *et al.*, Nucl. Data Sheets **123**, 135 (2015).

[38] K. J. Kelly, M. Devlin, J. M. O'Donnell, D. Neudecker, and E. A. Bennett, Nucl. Instrum. Methods A **1010**, 165552 (2021).

[39] R. Capote, Y.-J. Chen, F.-J. Hambsch, N. V. Kornilov, J. P. Lestone, *et al.*, Nucl. Data Sheets **131**, 1 (2016).

[40] C. J. Werner, J. Armstrong, F. B. Brown, J. S. Bull, L. Casswell, *et al.*, LA-UR-17-29981 (2017).

[41] C. J. Solomon, C. Bates, and J. Kulesza, LA-UR-17-21779 (March 30, 2017).

[42] R. Gold, Argonne National Labraory Report ANL-6984 (1964), 10.2172/4634295.

[43] M. Devlin, J. A. Gomez, K. J. Kelly, R. C. Haight, J. M. O'Donnell, *et al.*, Nucl. Data Sheets **148**, 322 (2018).

[44] A. Negret, Priv. Comm. (2022).

[45] K. Gul, M. Anwar, M. Ahmad, S. M. Saleem, and N. A. Khan, Phys. Rev. C **24**, 2458 (1981).

[46] D. Spaargaren and C. C. Jonker, Nucl. Phys. A **161**, 354 (1971).

[47] R. Bouchez, J. Duclos, and P. Perrin, Nucl. Phys. **43**, 623 (1963).

[48] R. L. Clarke and W. G. Cross, Nucl. Phys. **53**, 177 (1964).

[49] J. B. Singletary and D. E. Wood, Phys. Rev. **114**, 1595 (1959).

[50] J. D. Anderson, C. C. Gardner, J. W. McClure, M. P. Nakada, and W. C., Phys. Rev. **111**, 572 (1958).

[51] A. J. Plompen, O. Cabellos, C. De Saint Jean, M. Fleming, A. Algora, *et al.*, Eur. Phys. J. **56**, 181 (2020).

[52] Z. Ge, R. Xu, H. Wu, Y. Zhang, G. Chen, *et al.*, EPJ Web. Conf. **239**, 09001 (2020).

[53] K. Shibata, O. Iwamoto, T. Nakagawa, N. Iwamoto, A. Ichihara, *et al.*, J. Nucl. Sci. Technol. **48**, 1 (2011).

[54] G.M. Hale, Nucl. Data Sheets **109**, 2812 (2008).

[55] S. A. Kuvin, H. Y. Lee, B. DiGiovine, A. Georgiadou, S. Mosby, *et al.*, Phys. Rev. C **104**, 014603 (2021).